Ecosystem Health and Sustainability
A SCIENCE PARTNER JOURNAL

RESEARCH ARTICLE

Spatiotemporal Dynamics and Cross-Regional Effects of Wind Erosion Prevention Services in Typical Arid–Semiarid Zone

Huilin Zhang[1], Zhitao Wu[1*], Keming Ma[1,2], Hanxue Liang[1], Tianjie Lei[3], Ziqiang Du[1], and Xin Chen[1]

[1]Institute of Loess Plateau, Shanxi University, Shanxi 030006, China. [2]Research Center for Eco-Environmental Sciences, Chinese Academy of Sciences, Beijing 100080, China. [3]Institute of Environment and Sustainable Development in Agriculture, Chinese Academy of Agricultural Sciences (CAAS), Beijing 100081, China.

*Address correspondence to: wuzhitao@sxu.edu.cn

Citation: Zhang H, Wu Z, Ma K, Liang H, Lei T, Du Z, Chen X. Spatiotemporal Dynamics and Cross-Regional Effects of Wind Erosion Prevention Services in Typical Arid–Semiarid Zone. *Ecosyst. Health Sustain.* 2025;11:Article 0449. https://doi.org/10.34133/ehs.0449

Submitted 18 June 2025
Revised 24 September 2025
Accepted 5 November 2025
Published 9 December 2025

Wind erosion prevention service (WEPS) is critical for mitigating soil erosion and desertification in China's arid–semiarid zones. However, most existing studies have overlooked the spatial flow of WEPS, particularly the interannual variability and seasonal dynamics of sand transport pathways. This study focused on the loess hilly–gully region (LHGR), a climate-sensitive zone with intensified aeolian activity. We quantified the spatiotemporal dynamics of WEPS from 2000 to 2020 and simulated sand transport trajectories to assess cross-regional effects and socioeconomic dynamics. The results showed a marked increase in WEPS, indicating improved capacity of wind erosion prevention, with persistently high-value zones concentrated in northwestern arid regions such as the Mu Us Sandy Land. Wind trajectory identified 2,783 transport paths, dominated by spring winds (57.96%), which carried dust eastward toward densely populated areas and transboundary regions like Japan. Beneficiary areas exhibited a concentric spatial pattern, covering 599.96×10^4 km² (62.5% of China). The growing population, gross domestic product, and ecosystem service value highlighted its dual role in safeguarding human health and supporting sustainable development. Fraction vegetation coverage (FVC) emerged as the dominant factor for actual wind erosion by increasing surface roughness, with China's ecological restoration policies amplifying this function. Precipitation (PRE) predominantly regulated potential wind erosion, while synergistic interactions between FVC, PRE, and other drivers underscored the necessity for multi-factor governance. Our framework integrating physical flow and beneficiary mapping provides practical insights for optimizing payment for ecosystem service to enhance cross-regional ecological benefits.

Introduction

Ecosystem services (ESs), as critical links between natural capital and human well-being [1], have become a central focus in geography and ecology [2]. Compared with static valuation approaches, ES flow analysis enables the mapping of service transmission dynamics through flow pathways, directional vectors, and spatial extents, thereby establishing critical connections between service provision areas (SPAs) and service beneficiary areas (SBAs) [3]. In arid and semiarid regions, wind erosion prevention service (WEPS) is a critical regulating service that reduces aeolian sediment transport through surface cover [4]. The WEPS is beneficial not only for the local area but also for the downwind regions. This is clearly illustrated by severe sand and dust storms originating from northwest China [5], which pose significant threats to human health in north and northeast China, as well as in neighboring countries and regions such as Japan, Republic of Korea, Democratic People's Republic of Korea, the North Pacific, and North America [6]. Therefore, accurately delineating transmission pathways of WEPS is essential for understanding sand transport processes and optimizing hazard mitigation strategies.

Early wind erosion models, such as the wind erosion equation (WEQ), provided a foundation for research but were constrained by limited applicability across diverse environments and by their inability to represent complex factor interactions [7]. The Texas erosion analysis model (TEAM) represented an initial step toward integrating theoretical and empirical components; however, it lacked dynamic representation of erosion drivers, precluding its development as a fully process-based model [8]. The wind erosion assessment model (WEAM) offers field-scale estimates of sand drift and dust emissions but incorporates only 4 variables [8]. The wind erosion prediction system represented a significant advance as a process-based model capable of simulating daily weather, field conditions, and erosion events. Nevertheless, its substantial data and parameter demand restrict its application beyond field and watershed scales [9]. In comparison, the revised wind erosion equation (RWEQ) combines empirical relationships with process-based elements [10], representing meteorological conditions, vegetation cover, soil properties, field length, and management practices. RWEQ has been applied across multiple scales—from regional assessments in northern China [11] to global analyses [9]—and performs reliably under diverse climates, particularly in regions with annual precipitation ranging from 191 to 915 mm [12]. Accordingly, RWEQ serves as an effective tool for assessing reductions in wind erosion.

The flow mechanisms of different ES types are various. For WEPS, it reflects the quantity of sand transported by wind between the atmosphere and surface. To quantify sand transport pathways, we employed the hybrid single-particle Lagrangian integrated trajectory (HYSPLIT) model, developed by the National Oceanic and Atmospheric Administration (NOAA). HYSPLIT is widely used for simulating the transport, dispersion, and deposition of airborne particles due to its robust cross-scale capability and computational efficiency [13]. The model is based on a Lagrangian framework, which assumes that particles are advected by wind, with trajectories calculated through iterative integration of position vectors over time and space [14]. Owing to its strong broad applicability and ease of use [15], HYSPLIT is particularly appropriate for simulating WEPS flow paths and delineating beneficiary areas. For instance, Gao et al. [16] demonstrated the utility of HYSPLIT in delineating SPAs, SBAs, and sand transport across China's grasslands. Similarly, Xu et al. [15] and Su et al. [17] integrated RWEQ with trajectory clustering to visualize WEPS flow dynamics. However, there are few studies on the flow characteristics and benefit areas of WEPS in the arid–semiarid zone.

The loess hilly–gully region (LHGR) of China, a semi-arid and ecologically fragile area, has experienced significant ecological transformations in recent decades [18]. Despite its critical position in China's "Grain-for-Green" program and high susceptibility to wind erosion, research on WEPS in this region remains limited. Existing studies predominantly focus on static spatial analyses, neglecting temporal heterogeneity in the flow path of WEPS like interannual variation and seasonal differences [16]. To bridge these gaps, this study establishes a comprehensive framework for mapping the flow path of WEPS, with 4 primary objectives: (a) quantify the physical quantity of WEPS in the LHGR from 2000 to 2020 using the RWEQ model and analyze the spatiotemporal characteristic; (b) identify dominant drivers of AWE (actual wind erosion) and PWE (potential wind erosion) using geographical detector analysis; (c) simulate flow trajectories across multi-scale, ranging from interannual to seasonal via HYSPLIT; and (d) map beneficiary areas and evaluate their cross-regional effects. Our findings provide actionable insights for optimizing ecological restoration strategies and designing transboundary for PES (payment for ecosystem services), ultimately supporting sustainable management of fragile ecosystems of the LHGR.

Materials and Methods

Study area

As a representative geomorphic unit of the Loess Plateau [19], the LHGR is located in a climatic transitional zone between temperate semi-arid and semi-humid areas (Fig. 1). The region contains the national water and soil conservation ecological protection area in its central part and the windbreak and soil stabilization conservation ecological protection area in its northwestern part. These areas encompass key geomorphic units such as the Mu Us Sandy Land, Hunshandake Sandy Land, Yinshan Mountains, and Ordos Plateau. However, high annual evaporation, ranging from 1,000 to 1,500 mm/a, results in a persistent water deficit, thereby intensifying aeolian erosion processes. Land cover is primarily composed of grassland (40.37%) and cultivated land (32.31%). Historical deforestation, overgrazing, and unsustainable land reclamation have caused vegetation degradation. The vegetation degradation is further exacerbated by ongoing anthropogenic pressures, including agricultural expansion and infrastructure development. These multifactorial challenges present substantial obstacles to achieving sustainable development goals in the region.

Data sources

This study utilized multi-source datasets to assess the amount, transport trajectories, and beneficiary areas of WEPS. Data categories contained meteorological parameters, topography, land use and cover change, soil physicochemical properties, snow depth, vegetation cover, socioeconomic indicators, and atmospheric reanalysis variables. Detailed descriptions of these datasets, including sources, spatial and temporal resolution, and access information, are listed in Table S1. All spatial data layers were subjected to standardized preprocessing procedure including (a) resampling to 1-km spatial resolution, (b) projection unification to Albers equal-area conic projected coordinate system with WGS-1984 sphere, and (c) spatial alignment through raster registration.

Research framework

This study establishes an integrated framework combining multiple models for the assessment of the flow of WEPS. First, using multi-source datasets encompassing meteorological, topographic, vegetation, and soil parameters, we employ the RWEQ model to quantify the spatiotemporal dynamics of WEPS across the LHGR from 2000 to 2020, revealing its interannual variations and spatial heterogeneity patterns. Subsequently, the geographical detector model is employed to reveal the interactive mechanisms of driving factors arising from both natural and anthropogenic disturbances. Furthermore, we use the HYSPLIT model to simulate the flow path of WEPS at interannual and seasonal scales for the past 21 years and found the primary paths using Euclidean distance clustering from numerous trajectories to further analyze the major destinations of aeolian sand spread. Finally, we analyze the spatiotemporal differentiation of population, gross domestic product (GDP), and ecosystem service value (ESV) in beneficiary areas through overlay analysis. This framework provides scientific evidence for optimizing cross-regional ecological compensation policies and promoting sustainable development decision-making (Fig. 2).

Method

Estimation physical quantity of WEPS

The RWEQ framework incorporates weather factors, soil erodibility, soil roughness, and composite surface roughness, with equations expressed as [20]:

$$G = SL_{\mathrm{r}} - SL \quad (1)$$

where G denotes the physical quantity of WEPS (kg/m^2). SL_r and SL denote PWE and AWE (kg/m^2), respectively. The specific formula is as follows:

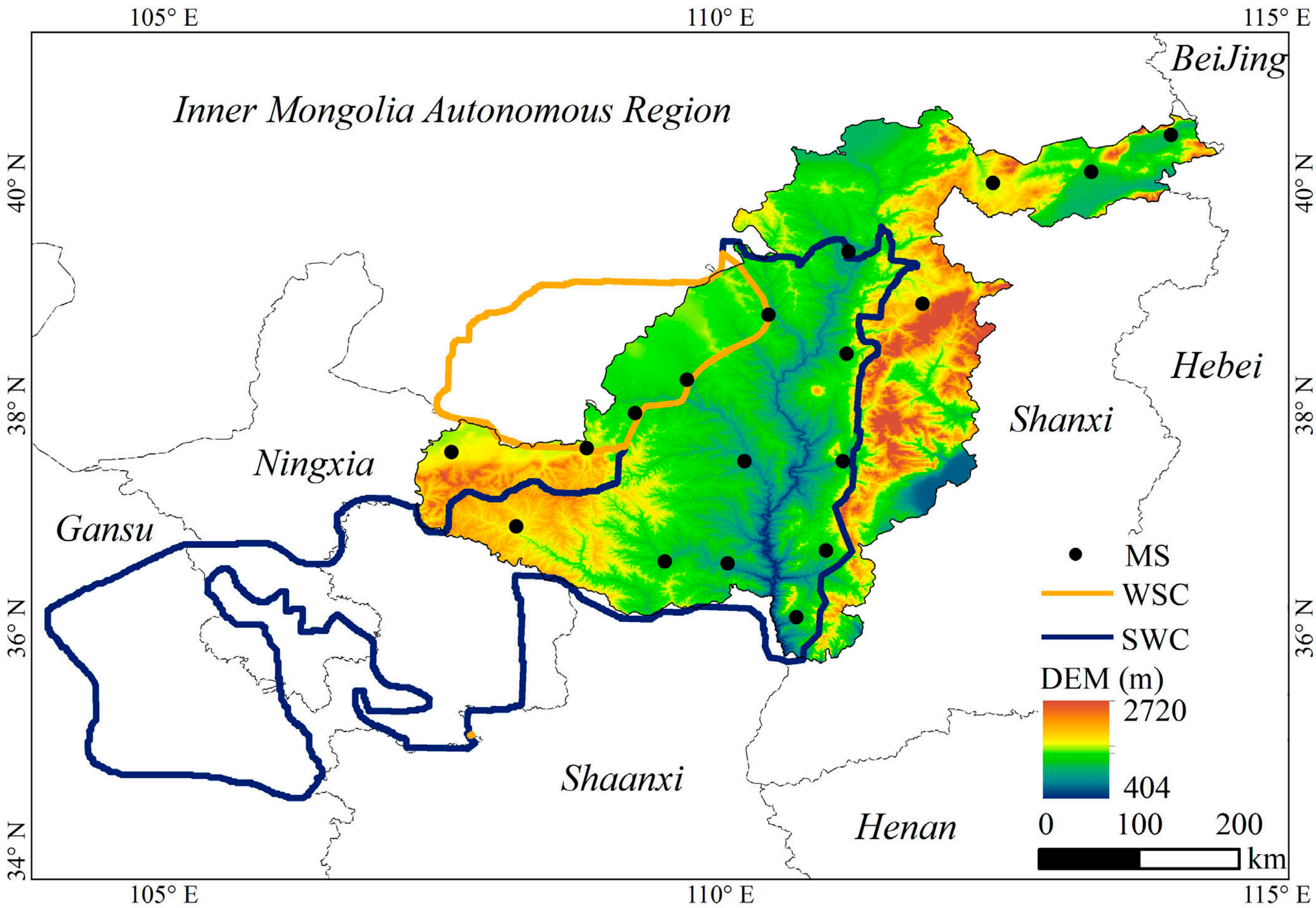

Fig. 1. Location of the loess hilly–gully region (LHGR). MS, Meteorological Station; SWC, Soil and Water Conservation Ecological Protection Area; WSC, the National Water and Soil Conservation Ecological Protection Area.

$$SL_r = \frac{2z}{S_r^{\,2}} Q_{r\max} \cdot e^{-(z/S_r)2} \quad (2)$$

$$SL = \frac{2z}{S^2} Q_{\max} \cdot e^{-(z/S)2} \quad (3)$$

where Q_{rmax} and Q_{max} are the maximum potential sediment transport capacity and the maximum sediment transport capacity (kg/m), respectively; S_r and S are the potential critical plot length and the critical plot lengths (m), respectively; and z is the calculated downwind distance (m), which is generally 50 m [21]. The specific formula is as follows:

$$Q_{r\max} = 109.8 \times \left(WF \times EF \times SCF \times K'\right) \quad (4)$$

$$S_r = 150.71 \times \left(WF \times EF \times SCF \times K'\right)^{-0.3711} \quad (5)$$

$$Q_{\max} = 109.8 \times \left(WF \times EF \times SCF \times K' \times C\right) \quad (6)$$

$$S = 150.71 \times \left(WF \times EF \times SCF \times K' \times C\right)^{-0.3711} \quad (7)$$

where WF is the weather factor (kg/m), EF is the soil erodibility fraction (dimensionless), SCF is the soil crust factor (dimensionless), K' is the surface roughness factor (dimensionless), and C is the combined crop factor (dimensionless). Detailed information is shown in Text S1.

Simulation of the flow paths of the WEPS

This study utilized the HYSPLIT model to calculate the trajectories of sand particle movement and track their flow directions, thereby effectively simulating the spatial flow paths of WEPS. Specifically, when wind speeds exceeded 5 m/s at the sand wind sites in the LHGR [22], these locations were set as the starting points for the simulation. Using NCEP (National Center for Environmental Prediction) reanalysis data, we simulated 5-d (120 h) forward trajectories of air parcels to represent dust uplift. The final position was determined based on the average velocity between the initial and first-guess positions.

The first predicted position is calculated as follows:

$$P'(t+\Delta t) = P(t) + V\left(p,t\right) + \Delta t \quad (8)$$

The final position is calculated as follows:

$$P(t+\Delta t) = P(t) + 0.5 \times \left[V\left(p,t\right) + V\left(p',t+\Delta t\right)\right] + \Delta t \quad (9)$$

where $P(t)$represents the initial position, $V(p,t)$ represents the velocity vector at the initial position, Δt represents the integration time step, and $V\left(p',t+\Delta t\right)$ represents the velocity vector at the first predicted position.

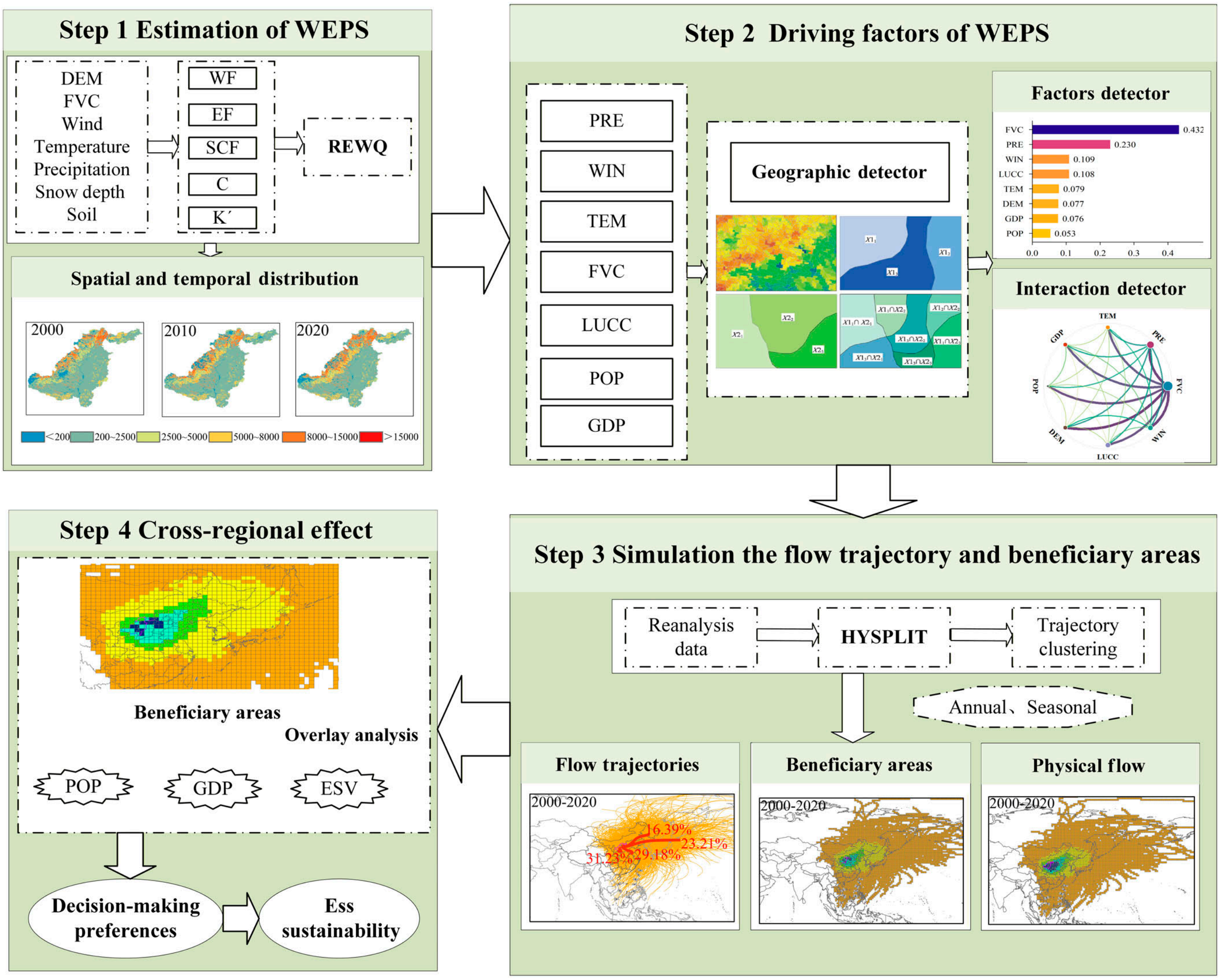

Fig. 2. Overall framework of this study.

Trajectory clustering

The TrajStat module of MeteoInfo software was employed, utilizing the angular distance method for cluster analysis [23]. The clustering process followed the criterion of significant increases in total spatial variation (TSV) among trajectories simulated by HYSPLIT, enabling the identification of major dust transport pathways.

Identification of the WEPS beneficiary area

Since the WEPS is an invisible protective service, its beneficiary areas should be identified as those most likely to be affected by sand and dust, namely, the areas that the dust diffusion paths pass through [24]. The spatial extent of these beneficiary areas can then be derived through sand dispersal trajectory interpolation. Using HYSPLIT-modeled trajectories, the frequency distribution module (or an equivalent command-line utility) within HYSPLIT generates trajectory density maps at a 1° × 1° grid resolution [15]. The method for calculating grid trajectory distribution frequency is as follows:

$$P_{ij} = \frac{L_{ij}}{\sum_{j=1}^{n} L_{ij}} \tag{10}$$

where P_{ij} is the simulated WEPS trajectory's distribution frequency of the jth grid in the ith year, L_{ij} is the number of simulated trajectories through the jth grid in the ith year, and n is the line number of all trajectories in the ith year.

Quantification of physical flow

Physical flow refers to the reduction in wind erosion due to vegetation cover. Under the influence of WEPS, a portion of dust that would otherwise be transported by wind is instead retained at its source. Consequently, this portion of dust is prevented from being transported to beneficiary areas, and thereby mitigating potential impacts on both residents and local ecosystems. The flow paths of WEPS are calculated based on a scenario assuming that no such services exist, which indicates how dust would spread without these services. The higher the distribution frequency of these service flow paths, the greater the material flow volume [13].

$$PL_i = G \times \frac{L_i}{L} \tag{11}$$

where G represents the physical amount of WEPS (kg/m^2), and L_i and L represent the path number on grid i and the total quantity of simulated paths, respectively.

The trend analysis of WEPS

To delineate multidecadal patterns in WEPS trajectories, this study adopted Theil–Sen median slope (denoted by α) for analyze trends in time-series data and the Mann–Kendall test (denoted by β) for characterize the significance of time-series trends [25]. The significance of the trend of time-series data is determined at the 95% confidence level, and the classification criteria of the trend are shown in Table S2.

The driving factor analysis of WEPS

The geographic detector provides a novel methodology for analyzing and interpreting spatiotemporal divergence patterns. Compared to other methods, the geodetector model particularly excels at analyzing factor interaction [26]. The methodology's theoretical foundation quantifies the explanatory power of independent variables by evaluating the covariation between dependent–independent variable spatial patterns through stratified variance analysis. In this study, the geographic detector model is applied to quantify the impact of natural factors and human activity factors on the AWE and PWE. Seven factors were selected for analysis: temperature (TEM), precipitation (PRE), fraction vegetation coverage (FVC), wind speed (WIN), population (POP), GDP, DEM, and land use (LUCC).

Results

Spatial and temporal distribution of WEPS

The physical quantity of WEPS in the LHGR showed an overall increasing trend from 2000 to 2020 (Fig. 3A), with the total amount fluctuating between 4.97×10^8 t and 6.7×10^8 t, with a mean annual value of 5.95×10^8 t. The maximum and minimum values occurred in 2019 and 2003, respectively. The quantity of WEPS per unit area ranged from 2,448.23 to 3,332.29 t/km², with an annual mean of 2,932.76 t/km². Spatiotemporal analysis revealed distinct geographical patterns, with the quantity of WEPS per unit area decreasing from northwest to southeast in the years 2000, 2010, and 2020 (Fig. 3B to D). The highest values were consistently observed in northwestern arid zones, specifically the Mu Us Sandy Land, characterized by sandy land cover and strong winds. The high WEPS (exceeding 8,000 t/km²) included Qing Shui He Country, He Lin Ge'er County, Yu Yang District, Shenmu City, and Zhungeer Banner.

Temporally, the mean annual WEPS per unit area increased from 2,703.24 t/km² in 2000 to 2,878.95 t/km² in 2010, and further to 3,152.17 t/km² in 2020. Over this period, significant spatial dynamics emerged in southwestern areas. Specifically, Dingbian County displayed a fluctuating pattern: WEPS intensity was initially low (<200 t/km²) in 2000, increased to moderate levels (200 to 2,500 t/km²) by 2010, and subsequently declined, with most areas returning to <200 t/km² by 2020. Conversely, Hengshan County exhibited an increased trend in the quantity of WEPS, rising from less than 200 t/km² in 2,000 to between 2,500 and 5,000 t/km² by 2020.

Pixel-level trend analysis of WEPS for 2000 to 2020 (Fig. 3E) revealed improvement trends across the study area. Specifically, 57.86% of the region showed an increasing trend, including 21.32% with significant improvement, primarily concentrated in the central zone. Conversely, a decreasing trend was observed in 37.94% of the region. This trend was classified as insignificant degradation and was mainly clustered in the southeast. Only 4.36% of the total area showed a significant degradation, predominantly located in the southeastern part of the eastern zone.

Driving factors of WEPS

The spatial scale of WEPS was divided into 1, 3, 5, 8, and 10 km. The 90% quantile of the explanatory variable's q value reached its maximum at 5 km (Figs. S1 and S2), identifying 5 km as the optimal spatial scale for both PWE and AWE. Factor detection showed that FVC was the strongest explanatory factor for AWE, contributing over 45%, followed by PRE (25%). WIN and LUCC both contributed around 10%, while the remaining factors had relatively minor explanatory power, each below 10% (Fig. 4A). For PWE, PRE was the dominant factor, accounting for 20% of the explanatory power, followed by wind speed at 11%. The remaining factors contributed less than 10%, exhibiting limited explanatory power (Fig. 4B). Interaction analysis of driving factors (Fig. 4C and D) revealed 2 distinct synergistic mechanisms: dual-factor enhancement and nonlinear enhancement, with no weakening or independent relationships. This indicated interconnected and mutually reinforcing effects among all factors influencing both AWE and PWE. For AWE, FVC exhibits the most pronounced interactive effects with other drivers. All pairwise interactions involving FVC demonstrated dual-factor enhancement, with explanatory power exceeding 40%, underscoring its pivotal role in regulating regional wind erosion. PWE is predominantly governed by PRE, which displays the strongest synergistic interactions with other factors.

Flow trajectories of WEPS

The capacity of preventing wind erosion in the LHGR improved, as evidenced by a decreasing trend in trajectories from 2000 to 2020 (Fig. 5A). A cumulative total of 2,783 trajectories were identified, peaking at 220 trajectories in 2000 and a significant decline to 72 trajectories by 2019. Seasonal analysis showed that the majority of high-wind days exceeding the sand-moving wind speed predominantly occurred in spring (March to May), totaling 1,613 times, which accounted for more than half (57.96%) of all recorded events. In contrast, autumn (September to November) had the least records, with only 299 occurrences, representing 10.74% of the total. Additionally, winter (December to February) and summer ((June to August) accounted for only 19.87% and 11.43%, respectively.

The cumulative frequency distribution of trajectories across stations displayed a distinct U-shaped seasonal pattern, with peaks in spring and troughs in summer and autumn (Fig. 5B to E). In 2000, the peaks were concentrated in March, April, and May; in 2010, peaks shifted to March, April, and December; while in 2020, the highest number of occurrences was noted in April, May, and June. Overall, wind speeds exceeding the sand-moving threshold predominantly concentrated in spring, during which dust movement paths were most numerous, whereas they were least frequent in summer. Among the station, the station with the highest frequency of occurrences was Dingbian, with a total of 446 times, followed by Suide (408 times) and Tianzhen (342 times).

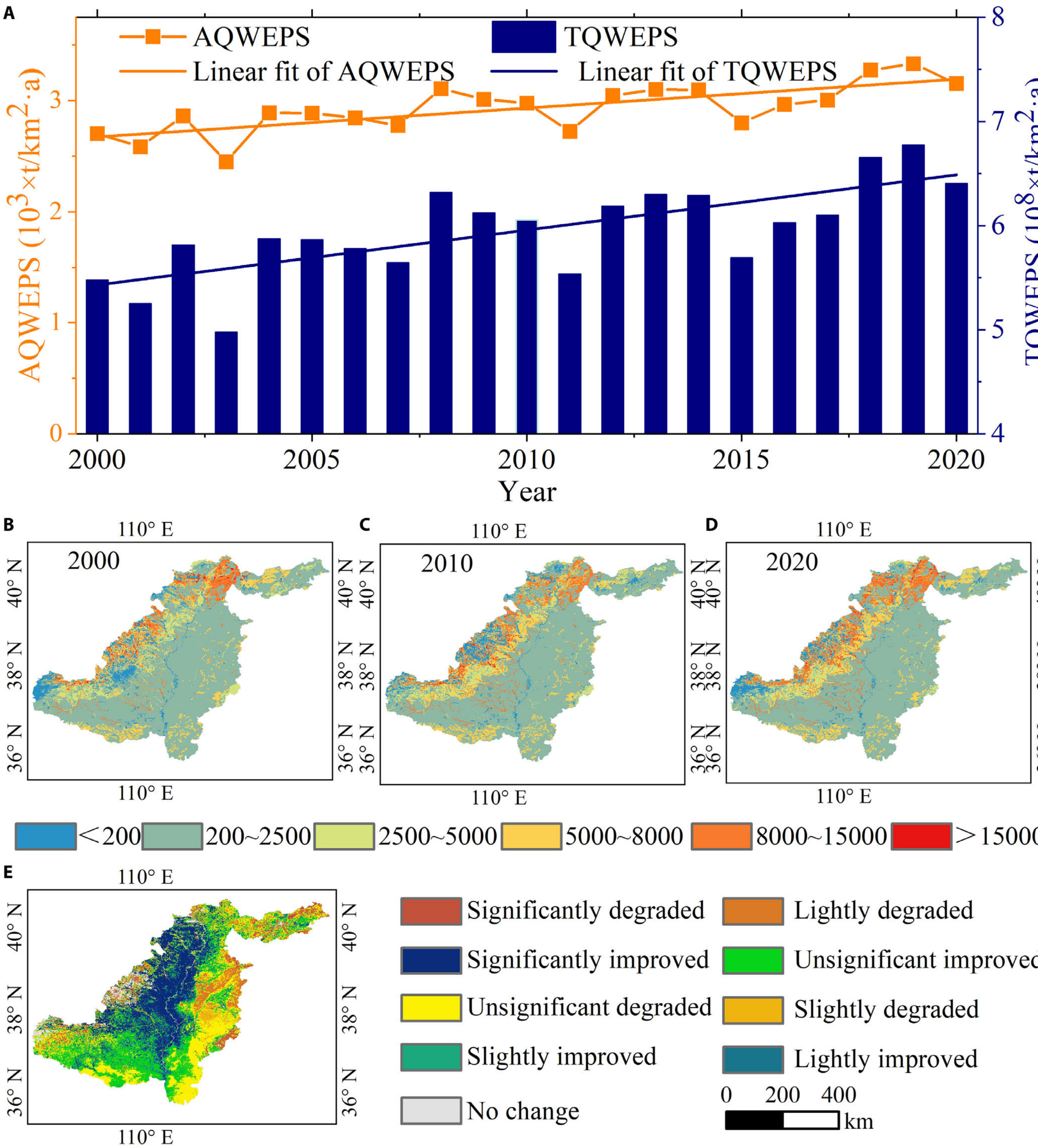

Fig. 3. (A) Total annual quantity and average quantity of WEPS from 2000 to 2020. AQWEPS, average quantity of WEPS per unit area; TQWEP, total quantity of WEPS. (B to D) Quantity of WEPS per unit area in the 2000, 2010, and 2020, respectively. (E) Significant trend of WEPS.

Trajectory transport paths analysis from 2000 to 2020 identified 4 dominant transmission routes (Fig. 6A): 31.23% of trajectories originated from the Mu Us Sandy Land, flowing southeastward along the Wuding River basin from Shaanxi to Shanxi, and are finally blocked by the Lvliang Mountains; 29.18% started from the northwest of Shanxi, crossing southern Hebei and Shandong, impacting Jiangsu Province; 23.20% also began from the northwest of Shanxi, passing through Hebei, Tianjin, Jilin, and Liaoning, extending to Japan; the final 16.39% traveled from the northwest of Shanxi through Hebei, Beijing, Inner Mongolia Autonomous Region, and Jilin, ultimately reaching Heilongjiang Province.

A gradual decline in trajectories was evident from 2000 to 2020 (Fig. 6B to D). In 2000, a total of 220 trajectories were simulated. Among them, 46.37% moved eastward through Beijing, Tianjin, and Liaoning, continuing along the Yellow Sea

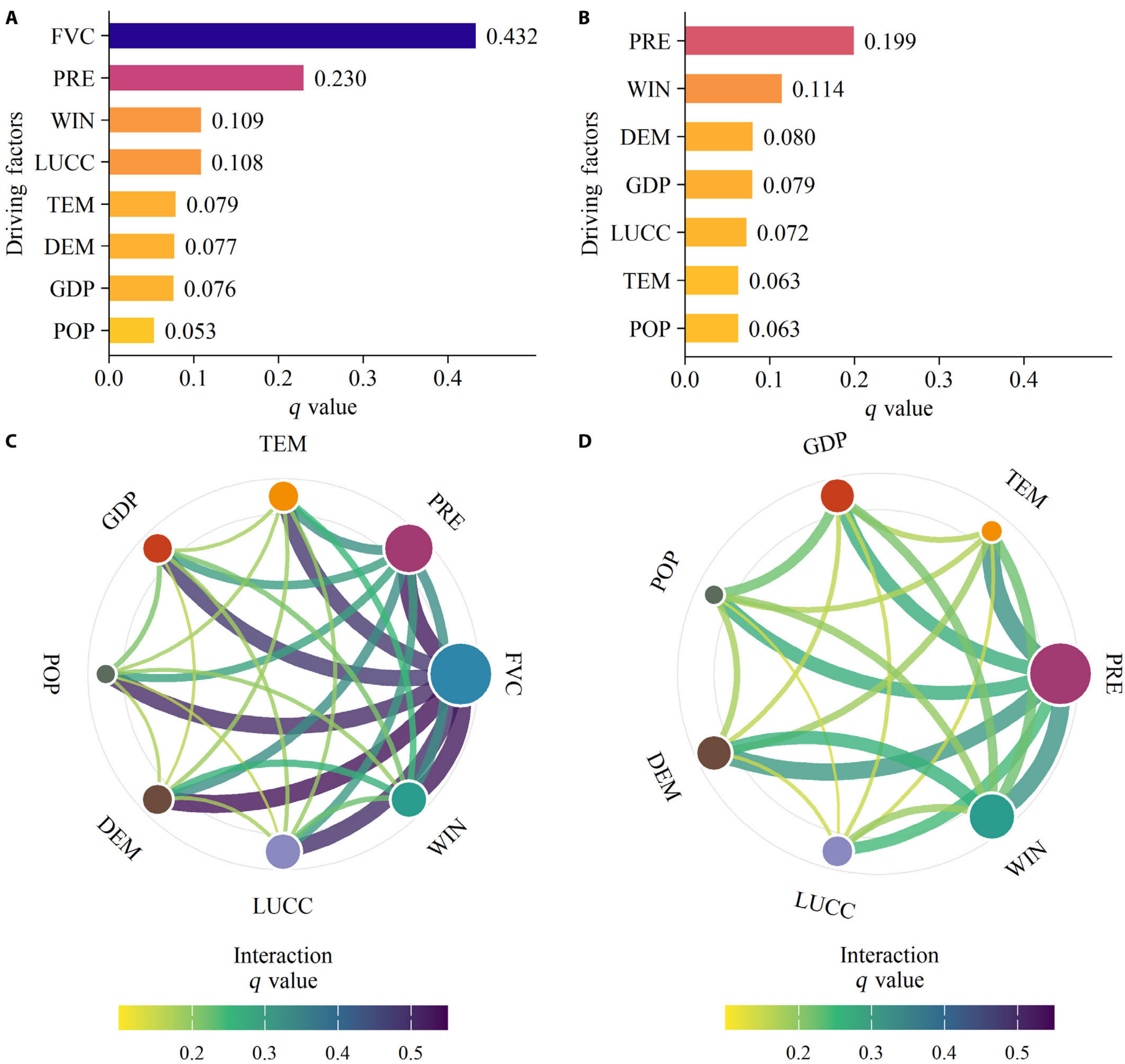

Fig. 4. (A) Single-factor average *q* value (2000, 2010, 2020) of AWE. (B) Single-factor average *q* value (2000, 2010, 2020) of PWE. (C) Interaction average *q* value (2000, 2010, 2020) of AWE. (D) Interaction average *q* value (2000, 2010, 2020) of PWE.

toward the Democratic People's Republic of Korea, Republic of Korea, and Japan; 27.27% flowed southeastward, primarily affecting domestic regions such as Shandong, Hubei, Henan, and Anhui, and the remaining 26.36% were restricted to internal areas, notably Shanxi and Shaanxi provinces. By 2010, the number of trajectories had declined to 189, which were predominantly concentrated in central and eastern provinces, with some extending to Russia, the Democratic People's Republic of Korea, the Republic of Korea, and Japan. By 2020, only 87 trajectories were recorded; of these, 58.62% were directed toward Henan and Shandong, 33.33% extended northeastward to Russia, and 8.05% drifted southward to Hubei and Hunan provinces.

Seasonal WEPS trajectories exhibited distinct patterns (Text S3 and Fig. S3). Spring, the most severe wind erosion season, showed that 83.25% eastward trajectories impact northeastern China, the Shandong Peninsula, North China Plain, and Japan, while 16.75% affect northwestern regions (Shaanxi, Gansu, and Shanxi). Summer trajectories were mainly northeastward, with 42.86% passing through Shanxi, Hebei, Tianjin, and Liaoning, and 15.76% extending to northern Japan. Autumn and winter trajectories were similar, with over half targeting Shanxi (autumn) or the Central Plains urban agglomeration (winter), and 12% to 16% extended across the Sea of Japan to Japan. Additionally, cross-sea transport into the Bohai Sea accounted for 29% to 33% of trajectories in both seasons.

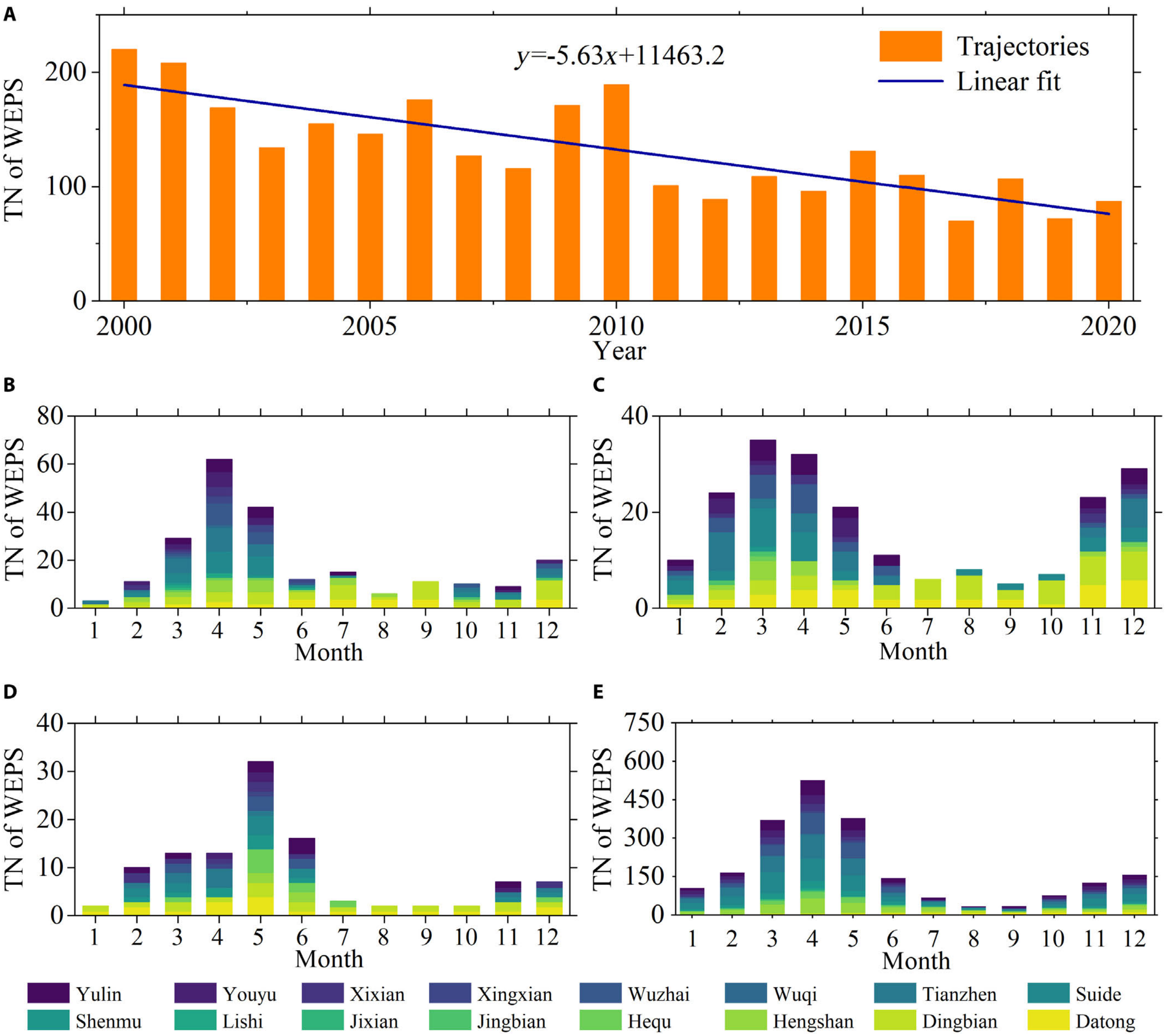

Fig. 5. (A) Trajectory number (TN) of WEPS from 2000 to 2020. (B to D) Trajectory number of the station in 2000, 2010, and 2020, respectively. (E) Trajectory number of the total station in 2000–2020.

Beneficiary areas of WEPS

The beneficiary areas of the WEPS for 2000 to 2020 were determined through spatial interpolation (Fig. 7). The frequency range of WEPS was divided into 5 intervals: 0% to 1%, 1% to 5%, 5% to 10%, 10% to 20%, and greater than 20% [16]. Trajectory frequencies exhibited a concentric pattern, with WEPS benefits diminishing radially outward from core zones, demonstrating clear distance decay. Analysis of WEPS beneficiary areas from 2000 to 2020 (Fig. 7A) revealed a total benefiting area of 566.25 $\times 10^4$ km^2, encompassing approximately 58.98% of China and extending to Republic of Korea, Democratic People's Republic of Korea, Japan, Mongolia, and portions of southern and eastern Russia.

High-frequency trajectory zones (>20% occurrence) accounted for only 2.35% of the total area, concentrated in Inner Mongolia Autonomous Region, Shanxi, Shaanxi, Hebei, and Beijing. In contrast, the lowest frequency category (<1%) covered 37.42% of the total area, predominantly affecting Heilongjiang, Gansu, Sichuan, Guangxi, Hunan, Shaanxi, and Jilin. Inner Mongolia Autonomous Region accounted for the largest proportion, followed by Gansu (Table S3). The total WEPS beneficiary areas in 2000, 2010, and 2020 were 1.32×10^7 km^2, 1.79×10^7 km^2, and 0.79×10^7 km^2, respectively (Fig. 7B to D). Among these, the benefited areas within China were 3.93×10^6 km^2, 4.4×10^6 km^2, and 3.59×10^6 km^2, accounting for 40.94%, 45.83%, and 37.34% of China's territorial area, respectively. This indicated a fluctuating trend of initial expansion followed by contraction. High-benefit frequency zones (>10%) remained concentrated in Shanxi, Shaanxi, Beijing, Tianjin, Hebei, and Henan, with frequencies exceeding 20% in parts of Hebei, Shaanxi, and Shanxi. Despite an increase in total benefiting area by 2010, the spatial extent of high-frequency zones diminished. Conversely, by 2020, while the total area declined, the spatial extent broadened significantly, extending southward to

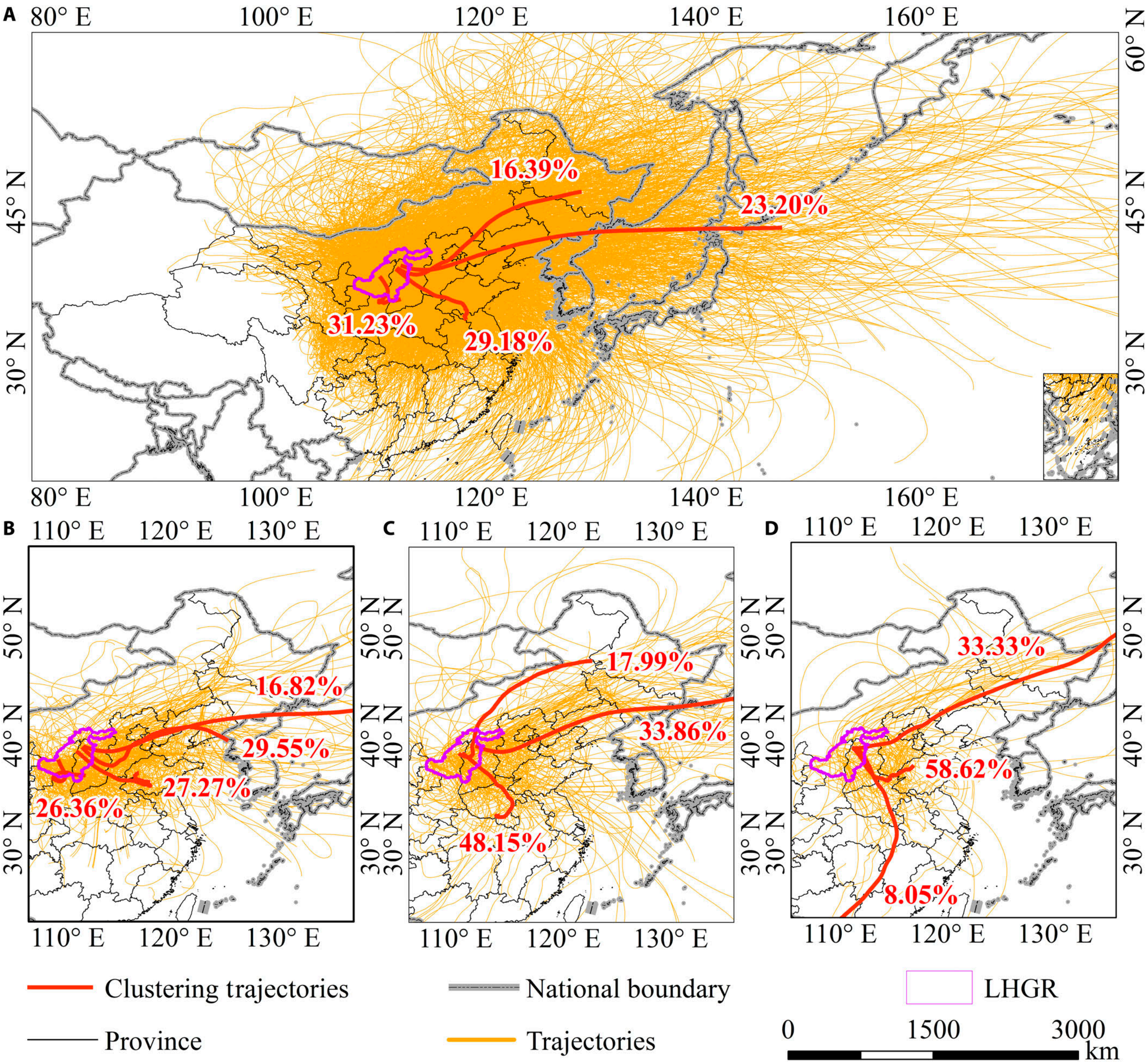

Fig. 6. Flow trajectories of WEPS (2000–2020): clustering analysis with Euclidean distance. (A) Number of WEPS flow trajectories from 2000 to 2020. (B to D) WEPS flow trajectories in 2000, 2010, and 2020, respectively.

encompass Guangxi and Guangdong provinces. The seasonal benefiting areas of WEPS were 3.71×10^7 km² (spring), 1.33×10^7 km² (summer), 1.76×10^7 km² (autumn), and 2.76×10^7 km² (winter) (Fig. S4).

We quantified the cross-regional socioeconomic and ecological effects of WEPS in the LHGR by integrating data on population, GDP, and ESV across beneficiary areas (Table 1). From 2000 to 2020, both the benefited population and the GDP showed increasing trends. The total benefited population was 894.8 million (72.01% of the national population) in 2000, 1,127.74 million (84.61%) in 2010, and 1,212.03 million (61.45%) in 2020. Meanwhile, GDP amounted to 7,038.19 billion yuan (68.72% of the national GDP), 29,234.61 billion yuan (86.93%), and 79,884.58 billion yuan (75.99%), respectively, while the ESV was 56.40 billion yuan (42.8%), 125.59 billion yuan (51.35%), and 110.31 billion yuan (41.57%). In 2000, areas with trajectory frequencies below 1% accounted for the largest shares of population, GDP, and ESV. However, by 2010 and 2020, the largest shares of population, GDP, and ESV were found in areas with trajectory frequencies between 1% and 5%. These results suggested that the WEPS in LHGR generated socioeconomic and ecological benefits nationwide—particularly in north and northeast China. Provinces such as Shanxi, Hebei, Beijing, Tianjin, Shandong, Henan, Liaoning, and western Inner Mongolia Autonomous Region had benefit trajectory frequencies greater than 5%. Areas with high-frequency distribution (>20%), such as Shanxi and Hebei, contributed relatively small proportions of the total beneficiary populations and GDP contributions. In contrast, areas with low-frequency distribution areas (<1%) accounted for the largest proportions.

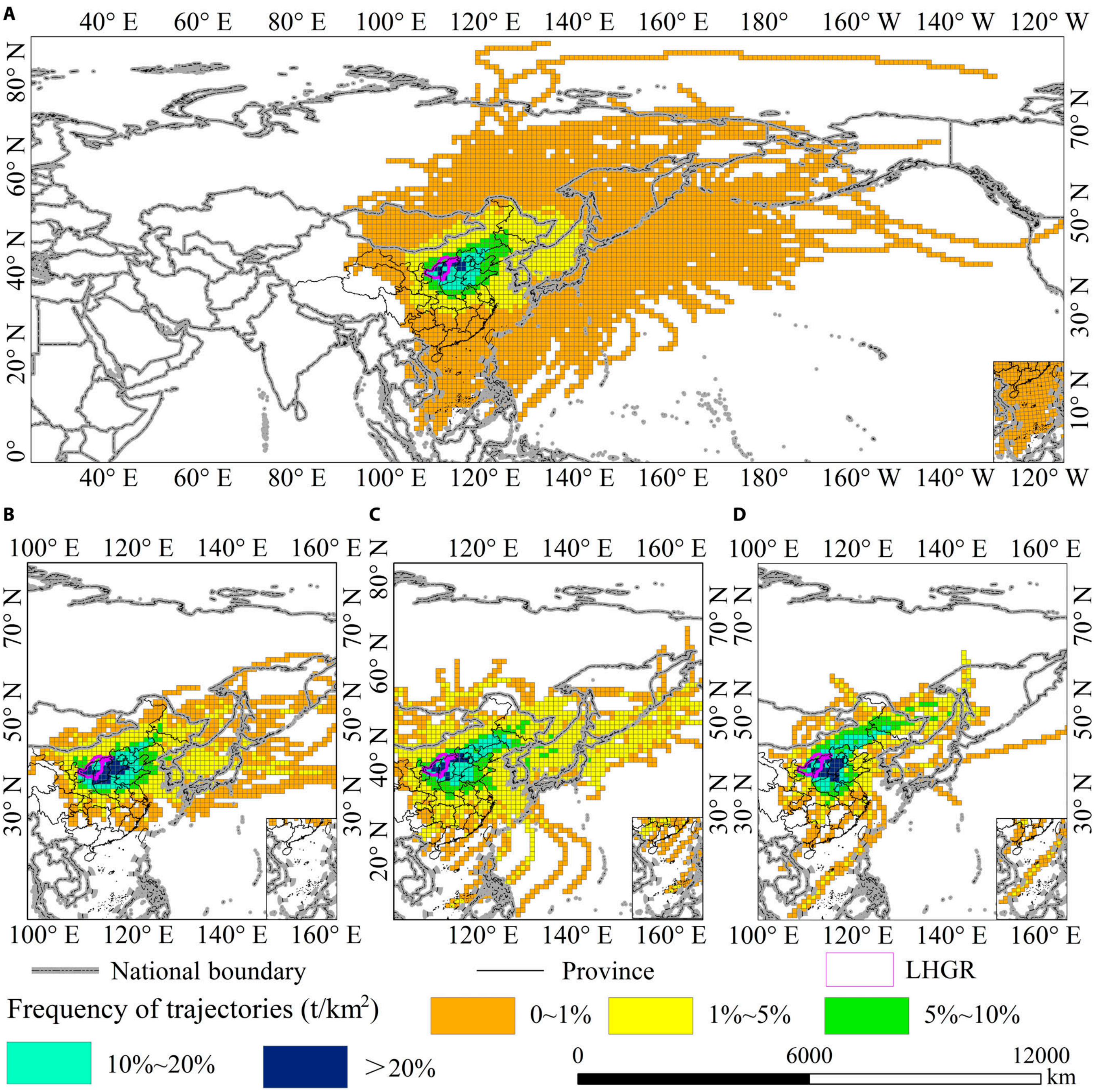

Fig. 7. (A) Beneficiary areas of WEPS from 2000 to 2020. (B to D) Beneficiary areas in 2000, 2010, and 2020, respectively.

This spatial mismatch can be attributed to the concentration of economic activities and dense populations in eastern regions.

Physical flow of WEPS

Based on the physical quantity of WEPS and the SBAs, the spatial distribution of the physical flow of the WEPS was determined. The total quantity of physical flow of WEPS in the LHGR was 12.6×10^9 t from 2000 to 2020, of which 9.19×10^9 t was received by domestic benefiting areas in China. The flow diminished concentrically outward from core regions—Shanxi, Hebei, Tianjin, and Beijing—exhibiting a radial distance–decay pattern (Fig. 8A).

The annual physical flow of WEPS in 2000, 2010, and 2020 was 5.6×10^8 t, 6.12×10^8 t, and 6.48×10^8 t, respectively. The proportion of areas with a WEPS capacity less than 0.1 t/km² was the largest, whereas areas exceeding 0.1 t/km² were mainly distributed in the east, indicating that the WEPS benefited the eastern part of the LHGR (Fig. 8B to D). Seasonally, WEPS physical flow peaked in spring (3.56×10^9 t) and reached its lowest level in summer (2.88×10^9 t). During spring, areas with WEPS below 0.5 t/km² were most widely distributed across the central and eastern regions of China. In contrast, during summer, the majority of WEPS concentrated in the northern regions of China (Text S5 and Fig. S6).

Table 1. Population, GDP, and ESV in the beneficiary areas from 2000 to 2020

Year	Beneficiary areas of WEPS	Population in the service beneficiary areas (million)	Percentage of the Chinese population (%)	GDP in the service beneficiary areas (billion yuan)	Percentage of the Chinese real GDP (%)	ESV in the service beneficiary areas (billion yuan)	Percentage of the Chinese ESV (%)
2000	<0.01	260.07	20.93	2,463.92	24.06	20.13	15.28
	0.01–0.05	213.82	17.21	1,797.81	17.55	19.34	14.68
	0.05–0.1	130.96	10.54	1,167.88	11.40	6.87	5.22
	0.1–0.2	192.75	15.51	1,506.42	14.71	6.51	4.94
	>0.2	972	7.82	102.16	1.00	3.55	2.69
	Total	849.8	72.01	7,038.19	68.72	56.40	42.8
2010	<0.01	225.46	16.92	5,446.43	16.19	27.03	11.05
	0.01–0.05	424.8	31.87	10,779.9	32.05	62.34	25.49
	0.05–0.1	217.56	16.32	5,772.54	17.16	18.28	7.47
	0.1–0.2	218.55	16.40	6,108.29	18.16	13.38	5.47
	>0.2	41.37	3.10	1,127.45	3.35	4.56	1.86
	Total	1,127.74	84.61	29,234.61	86.93	125.59	51.35
2020	<0.01	0	0.00	0.00	0.00	0.00	0
	0.01–0.05	782.33	39.66	54,350.98	51.70	71.88	27.09
	0.05–0.1	146.24	7.41	7,802.07	7.42	18.38	6.93
	0.1–0.2	175.83	8.91	12,747.06	12.13	14.53	5.48
	>0.2	107.63	5.46	4,984.46	4.74	5.53	2.08
	Total	1,212.03	61.45	79,884.58	75.99	110.31	41.57

Discussion

Verification of results

The estimated WEPS for LHGR during 2000–2020 was 2,932.76 t/(km^2·a), which is reasonably consistent with the values of 2,214 t/(km^2·a) reported by Li et al. [27] and 2,430 t/(km^2·a) reported by Fan et al. [28] in the Loess Plateau. However, our slightly higher estimates likely reflect unique topographic influences in the hilly–gully ecosystem. Specifically, the characteristic "canyon effect" in this terrain [29] may enhance wind acceleration, potentially intensifying erosional processes compared to plateau averages. Moreover, many researchers have corroborated the accuracy of the RWEQ by correlating soil erosion intensity with the frequency of dust storms [30]. In this study, we analyzed statistical data on the dust storm frequency on the Loess Plateau from 2000 to 2007 to validate the dynamic changes in wind erosion (Fig. 9A). The interannual analysis revealed consistency between the variations in WEPS capacity and dust storm frequency in the LHGR, reinforcing the reliability of temporal simulations of the RWEQ.

To validate the HYSPLIT simulation results, we used the MOD08_D3 aerosol optical depth (AOD) and PM_{10} observing data. Following Cuevas-Agulló et al. [31], we defined a desert aerosol event as one where the AOD values ranged between 0.18 and 0.33 and persisted at such levels for 3 consecutive days. On 2017 May 5 and 2019 May 19 (Fig. 9B to D), the trajectories transported southeast toward Hebei Province before recurving northeast to northeast China and the Korean Peninsula. As the dust was transported during the 3 events, AOD and PM_{10} levels increased markedly in areas coinciding with the trajectories, confirming the impact of dust transport. This consistency between our simulated trajectories and independent observations validates the accuracy of our simulation.

Furthermore, the results of seasonal trajectory clustering (Fig. S3) demonstrate that the clustered trajectories agree with the wind direction in the LHGR. During spring, the prevailing westerly to northwesterly winds, under the continuous influence of the Siberian High, induce atmospheric and soil aridity [32]. The persistent strong winds combined with dry surface conditions lead to frequent occurrence of dust storms, commonly known as "Yellow Dust". Consequently, spring had the highest frequency of dust transport trajectories, affecting a vast area of up to 3.71×10^7 km^2, including the Korean Peninsula and Japan. In the summer, the convergence of the East Asian and South Asian monsoons causes the prevailing wind direction to shift predominantly to southeasterly or southwesterly [33]. This flow brings warm, moist air that promotes precipitation and alleviates drought conditions, leading to a significant reduction in dust transport trajectories. As a result, the overall dust transport direction becomes mainly northeastward, decreasing the affected area. As autumn progresses, the strengthening of cold air masses causes the wind direction to shift from southeasterly to westerly and northwesterly. Wind speeds increase, accompanied by drier conditions, reduced precipitation, and diminished vegetation cover, which enhances wind erosion. Transport trajectories shift from a predominantly northeastward direction in summer to an eastward one. During winter, the Siberian high-pressure system dominates, with northwesterly winds that are strong, cold, and dry [34]. The lack of precipitation, combined with exposed ground surfaces, leads to significant wind erosion. Although the prevailing transport direction remains southeasterly, dust storms are less frequent

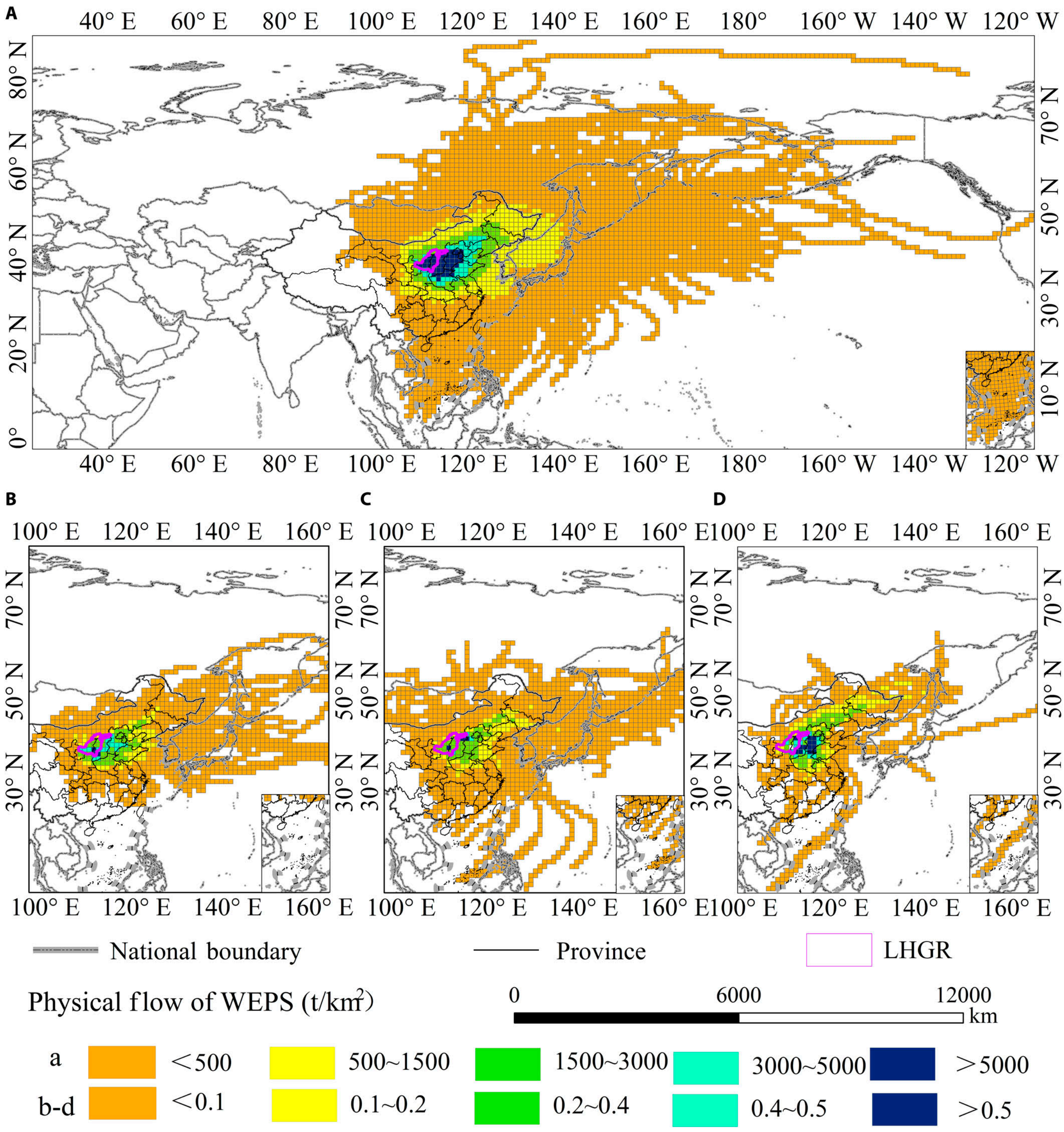

Fig. 8. (A) Physical flow of WEPS from 2000 to 2020. (B to D) Physical flow of WEPS in 2000, 2010, and 2020, respectively.

compared to spring, primarily due to frozen surfaces or snowpack. These seasonal transport dynamics underscore the complex interaction between synoptic systems [35], surface hydrology [36], and anthropogenic influences [37] in shaping regional dust transport patterns.

Drivers of changes affecting WEPS

Changes in WEPS are the result of the combined action of natural and human factors [15]. The findings demonstrate that FVC is the primary driver in AWE, highlighting that vegetation in this region plays a critical role in mitigating soil erosion [38]. First, vegetation prevents wind-induced soil erosion by increasing surface roughness and absorbing the downward momentum of airflow. Secondly, plants with lower branches decrease wind speeds near the ground surface and capture sediment particles [39]. Since the launch of China's ecological restoration projects in 2000, strategic interventions including the Three-North Shelter Forest Construction Project (TNP), the Grain for Green Project (GFGP), the Natural Forest Protection Project (NFP), and the Beijing–Tianjin Sand Source Control Project

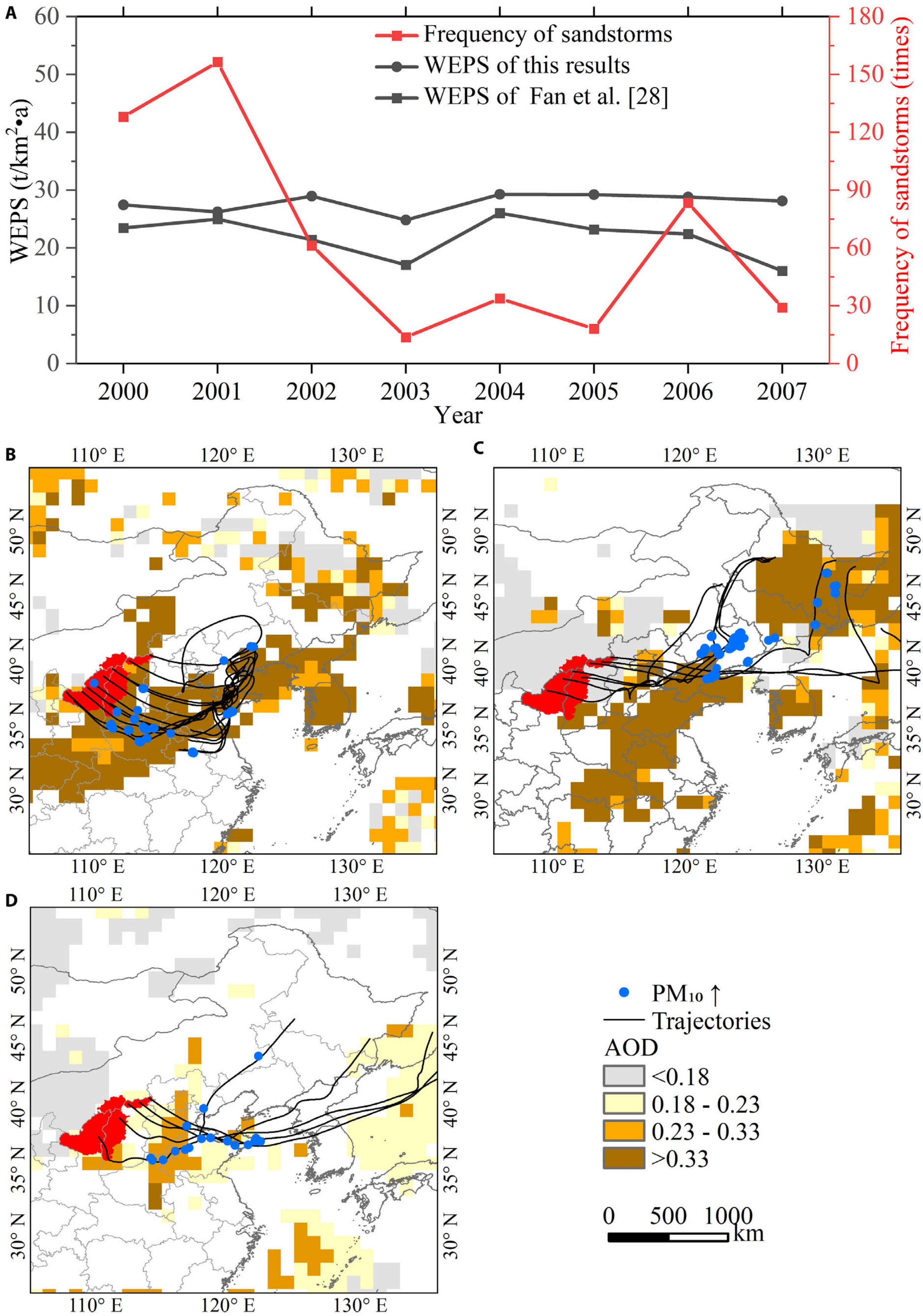

Fig. 9. (A) RWEQ model accuracy verification: the result of WEPS and Fan et al. [28] and dust storm frequency. (B to D) HYSPLIT model and the AOD outcomes of the 3 dust events: (B) 2015 June 10, (C) 2017 May 5, and (D) 2019 May 19. PM_{10}↑ showed the recorded higher concentrations compared to previous day on 3 dates.

(BTP) [40] have substantially modified vegetation patterns in the LHGR. Enhanced vegetation coverage emerges as a crucial nature-based mitigation strategy against soil wind erosion, particularly in spring. Our analysis demonstrates that wind erosion primarily occurs during spring when vegetation is in its initial growth stage, resulting in large areas with insufficient ground coverage where the inhibitory effect on wind erosion is not fully realized. The study further identifies precipitation as the dominant driver factor for PWE. Increased rainfall exhibits dual protective mechanisms: physically enhancing soil cohesion through moisture-mediated particle bonding [41], and biologically facilitating vegetation recovery via improved soil water availability [42]. This precipitation–vegetation synergy underscores the importance of integrated hydrological and ecological management strategies for comprehensive erosion control.

Policy implications of WEPS flow

By simulating the flow of WEPS in the LHGR, this study demonstrates that the ESs supplied and delivered by this region to downstream beneficiaries are critically important and possess substantial economic value. Wind erosion is characterized by long-distance transport [43]. Consequently, enhancing the WEPS in the LHGR not only mitigates local wind erosion but also generates significant ecological benefits for downstream regions, including the Beijing–Tianjin–Hebei area and the eastern coast of China, with positive effects extending to transboundary regions such as Mongolia and Japan. The quantitative assessment of the WEPS flow and patterns establishes a scientific basis for cross-regional ecological compensation policies. Horizontal payment is the highly equitable approach to implement ecological compensation [4]. Ecological compensation should not rely on a uniform standard but should instead be calibrated according to the actual flow of ESs and socioeconomic factors of beneficiary regions, such as GDP, population, and ESV. This approach operationalizes the beneficiary-pays principle, leading to more refined and equitable compensation criteria. The cross-regional effects of WEPS further indicate that wind erosion control must transcend traditional administrative boundaries to establish a cross-regional and collaborative governance framework across regions and even national borders [44]. There is an urgent need to develop a multi-level cooperation system encompassing data sharing, institutional coordination, and joint actions for addressing wind erosion as a cross-regional environmental issue in an integrated manner.

The ecosystems in the typical arid and semi-arid regions focused on in this study are particularly responsive to climate change due to their inherent ecological sensitivity and fragility [45]. In the future, the synergistic effects of climate change and human activities are projected to become the dominant driver of changes in the WEPS. A broad consensus in existing research indicates that future climate change will increase the frequency and intensity of extreme events including heavy rainfall, droughts, and wildfires [46]. These impacts are projected to be most severe under high-emission scenarios (e.g., SSP5-8.5) [47], whereas they would be significantly mitigated under low-emission scenarios (e.g., SSP1-2.6). These changes will directly or indirectly trigger multiple negative effects, leading to a decline in soil retention capacity and significantly increasing the risk of surface wind erosion. Furthermore, they will contribute to reduced vegetation coverage, degradation of community structure, and weakened sand fixation capacity provided by vegetation through increased surface roughness. This will also result in a diminished carbon sink function of ecosystems [48], potentially impairing the overall stability of ecosystems and their long-term ability to sustain critical ecological services such as wind erosion prevention. Therefore, ecological policies must pay close attention to the potential threats posed by different future climate scenarios. Adaptive management is integrated into ecological conservation policy design to enhance ecosystem resilience against climate risks.

Limitations and prospects

Simulating the spatiotemporal dynamics of large-scale wind erosion remains a persistent challenge in wind erosion studies, with no unified measurement scale framework currently available. In this study, we employed the RWEQ model to simulate wind erosion patterns over a 21-year period in the LHGR, with particular emphasis on quantifying the spatiotemporal variations of WEPS. However, the reliability of our simulations was constrained by the lack of field validation data, especially for input parameter uncertainties. For instance, wind speed data, a critical input for the RWEQ model, were generated through ANUSPLIN interpolation software using meteorological station observations with a local thin plate smoothing spline algorithm. While this methodological approach has been validated in previous studies [49], spatial interpolation uncertainties inherent to meteorological data processing remain exited. When selecting driver data for the HYSPLIT model, a trade-off between spatial resolution and temporal coverage must be considered. While the driving data (e.g., global data assimilation system and global forecast system) offer higher spatial resolution, their historical records do not cover the entire period from 2000 to 2020. The GBL (global boundary layer) reanalysis data provide a long-term and continuous time series, and had been widely validated and applied in studies such as dust transport [50]. This study ultimately employs the GBL data to ensure temporal completeness of the research period.

To address these limitations, future work should prioritize the integration of multi-scale field observations with process-based modeling frameworks. Such integrated approaches would significantly improve model parameterization accuracy. Furthermore, we will develop and apply coupled climate–vegetation–erosion models to simulate the evolution of WEPS under different future climate scenarios [e.g., shared socioeconomic pathways (SSPs)], which represents a key direction for our subsequent research.

Conclusion

Utilizing the RWEQ model, this study evaluated the spatiotemporal dynamics of WEPS in the LHGR from 2000 to 2020, revealing key insights regarding service flow transmission and cross-regional effects.

1. The physical quantity of WEPS exhibited a marked overall increase during the study period, indicating an enhanced regional capacity for wind erosion prevention. Spatially, the northwestern arid zones, particularly the Mu Us Sandy Land, demonstrated the highest WEPS values due to their sandy land cover and intense winds. This spatial heterogeneity emphasizes geomorphological–climatic coupling in wind erosion.
2. FVC was the dominant factor for AWE, primarily through dual mechanisms: increasing surface roughness and

reducing near-surface wind dynamics for trapping sediments. The implementation of China's ecological restoration projects has significantly amplified this protective function. PWE was predominantly regulated by PRE. Interaction analysis revealed that FVC and PRE serve as pivotal factors for AWE and PWE, respectively. Moreover, these key factors exhibited synergistic effects with other drivers, highlighting the necessity of integrated management strategies that consider multiple factors simultaneously.

3. A total of 2,783 trajectories were identified, with 3 dominant directions: 39.6% moving eastward/northeastward, 29.18% dispersing southward through southern Hebei and Shandong, ultimately reaching Jiangsu Province, and 31.23% circulating within the LHGR. Spring accounted for 57.96% of total trajectories (n = 1,613). Among these, 83.25% extended eastward to high-population zones, such as Shandong Peninsula and North China Plain, with some even reaching areas including Japan. These findings confirm spring as a crucial period for mitigating transboundary dust impacts.
4. The WEPS service flow covers beneficiary area of 599.96 × 10^4 km^2 (62.5% of China's territory), with Inner Mongolia Autonomous Region accounting for the largest proportion. Spatially, beneficiary zones exhibit a concentric circular structure centered on the LHGR, with the benefits decreasing radially following a distance–decay pattern. This flow pattern highlights the critical role of the LHGR in protecting downstream socioecological systems, particularly in regions such as Shanxi, Hebei, Tianjin, and Beijing. The increasing beneficiary population, GDP, and ESV highlight its benefits of WEPS in safeguarding human health, preserving ecosystems, and promoting sustainable economic development. This helps quantify the often-neglected socioeconomic benefits arising from regional wind erosion control.

Finally, this study reveals a pronounced spatial mismatch between WEPS "source" areas (LHGR) and downstream "sink" beneficiaries. It establishes a comprehensive framework for assessing the cross-regional flow benefits of WEPS, providing a theoretical foundation for ES management and policy-making.

Acknowledgments

Funding: This work was supported by the Shanxi Province Science and Technology Innovation Talent Team Special Grant (202204051001010), the National Natural Science Foundation of China (41977412), and the National Key R&D Program of China (2023YFF1305102).
Author contributions: H.Z.: Conceptualization, methodology, data curation, software, formal analysis, and writing—original draft. Z.W. and K.M.: Conceptualization, supervision, and writing—review and editing. H.L. and T.L.: Writing—review and editing. Z.D. and X.C.: Software and data curation. All authors have read and agreed to the published version of the manuscript.
Competing interests: The authors declare that they have no competing interests.

Data Availability

All data in this study are publicly available online. The codes used in this article are available by contacting the corresponding author.

Supplementary Materials

Texts S1 to S5
Tables S1 to S4
Figs. S1 to S6

References

1. Bagstad KJ, Johnson GW, Voigt B, Villa F. Spatial dynamics of ecosystem service flows: A comprehensive approach to quantifying actual services. *Ecosyst Serv*. 2013;4:117–125.
2. Peng J, Xia P, Liu Y, Xu Z, Zheng H, Lan T, Yu S. Ecosystem services research: From golden era to next crossing. *Trans Earth Environ Sustain*. 2023;1:9–19.
3. Wang D, Liang Y, Peng S, Yin Z, Huang J. Integrated assessment of the supply–demand relationship of ecosystem services in the Loess Plateau during 1992–2015. *Ecosyst Health Sustain*. 2022;8(1):2130093.
4. Pan J, Wei J, Xu B. Simulation of the spatial flow of wind erosion prevention services in arid inland river basins: A case study of Shiyang River Basin, NW China. *Atmos Res*. 2023;14(12):1781.
5. Song H, Zhang K, Piao S, Wan S. Spatial and temporal variations of spring dust emissions in northern China over the last 30 years. *Atmos Environ*. 2016;126:117–127.
6. Mikami M, Shi GY, Uno I, Yabuki S, Iwasaka Y, Yasui M, Aoki T, Tanaka TY, Kurosaki Y, Masuda K, et al. Aeolian dust experiment on climate impact: An overview of Japan-China joint project ADEC. *Glob Planet Change*. 2006;52(1-4):142–172.
7. Tatarko J, Sporcic MA, Skidmore EL. A history of wind erosion prediction models in the United States Department of Agriculture prior to the Wind Erosion Prediction System. *Aeolian Res*. 2013;10:9–24.
8. Webb NP, McGowan HA. Approaches to modelling land erodibility by wind. *Prog Phys Geogr*. 2009;33(5):587–613.
9. Sun R, He H, Jing Y, Leng S, Yang G, Lü Y, Borrelli P, Chen L, Fu B. Global wind erosion reduction driven by changing climate and land use. *Earth Future*. 2024;12:e2024EF004930.
10. Fryrear DW, Bilbro JD, Saleh A, Schomberg H, Stout JE, Zobeck TM. RWEQ: Improved wind erosion technology. *J Soil Water Conserv*. 2000;55(2):183–189.
11. Du H, Liu X, Jia X, Li S, Fan Y. Assessment of the effects of ecological restoration projects on soil wind erosion in northern China in the past two decades. *Catena*. 2022;215: Article 106360.
12. Seo IW, Lim CS, Yang JE, Lee SP, Lee DS, Jung HG, Lee KS, Chung DY. An overview of applicability of WEQ, RWEQ, and WEPS models for prediction of wind erosion in lands. *Korean J Agric Sci*. 2020;47(2):381–394.
13. Xu J, Xiao Y, Xie G. Interregional ecosystem services benefits transfer from wind erosion control measures in Inner Mongolia. *Environ Dev*. 2020;36:Article 100496.
14. Wang W, Li W, Wang J, Hao X. Water vapor from western Eurasia promotes precipitation during the snow season in northern Xinjiang, a typical arid region in Central Asia. *Water*. 2020;12(1):141.
15. Xu J, Xiao Y, Xie G, Wang Y, Jiang Y. Computing payments for wind erosion prevention service incorporating ecosystem services flow and regional disparity in Yanchi County. *Sci Total Environ*. 2019;674:563–579.
16. Gao X, Zhang H, Huang L, Fan J, Liu X, Cao W, Liu H, Liu G. Where, when, and how much should we pay for wind erosion

prevention services of the largest Chinese grassland reserve? *Environ Sci Technol*. 2024;58(6):2615–2626.
17. Su K, Sun X, Guo H, Long Q, Li S, Mao X, Niu T, Yu Q, Wang Y, Yue D. The establishment of a cross-regional differentiated ecological compensation scheme based on the benefit areas and benefit levels of sand-stabilization ecosystem service. *J Clean Prod*. 2020;270:Article 122490.
18. Liu Y, Huang X, Liu Y. Detection of long-term land use and ecosystem services dynamics in the Loess Hilly-Gully region based on artificial intelligence and multiple models. *J Clean Prod*. 2024;447:Article 141560.
19. Chen Z, Li Y, Liu Y, Liu X. Does rural residential land expansion pattern lead to different impacts on eco-environment? A case study of loess hilly and gully region. *China Habitat Int*. 2021;117:Article 102436.
20. Guo X, Wang T, Li Z, Zhang J, Yu K, Li P, Geng Y, Wu H, Ke G. Identification of dominant factors and scenario prediction of ecosystem services in the Jialing River basin. *China Ecosyst Health Sustain*. 2025;11:0361.
21. Li J, Yuan X, Su Y, Qian K, Liu Y, Yan W, Xu S, Yang X, Luo G, Ma X. Trade-offs and synergistic relationships in wind erosion in Central Asia over the last 40 years: A Bayesian network analysis. *Geoderma*. 2023;437:Article 116597.
22. Hu W, Wu X, Zhang K. Spatiotemporal change of beneficiary area from wind erosion prevention service in the Ulan Buh Desert in 2008 and 2018. *Geogr Sustain*. 2022;2(2):119–128.
23. Wang Y. MeteoInfo: GIS software for meteorological data visualization and analysis. *Meteorol Appl*. 2014;21:360–368.
24. Xu J, Xiao Y, Xie G, Wang Y, Lei G. Assessment of the benefit diffusion of windbreak and sand fixation service in National Key Ecological Function areas in China. *Aeolian Res*. 2021;52:Article 100728.
25. Yuan H, Yang R, Wu J, Zhang J, Zhou L. Vegetation productivity in Xinjiang's ecosystems: Responses to natural and human factors across basins and land covers. *Ecosyst Health Sustain*. 2025;11:0338.
26. Wang B, Che L, Dai C, Zheng L, Li Z, Wang X. The impacts of China's Shan-Shui Initiative on ecosystem services: A case study in the Three Gorges Reservoir Area. *Ecosyst Health Sustain*. 2025;11:0398.
27. Li Q, Li D, Wang S, Wang J, Wang R, Fu G, Yuan Y, Zheng Z. Spatiotemporal patterns and driving factors of soil protection in the wind-water erosion area of Chinese Loess Plateau. *J Arid Land*. 2024;16(11):1522–1540.
28. Fan K, Liu Y, Zhang X, Chen X, Li Y, Zhou Y, Shen W, Tao H, Gong C, Lei S. Assessing the relative contribution of climate change and human activity factors to spatiotemporal distributions of sand fixation service in the Loess Plateau. *GISci Remote Sens*. 2025;62(1):2444630.
29. Leenders JK, van Boxel JH, Sterk G. The effect of single vegetation elements on wind speed and sediment transport in the Sahelian zone of Burkina Faso. *Earth Surf Process Landf*. 2007;32(10):1454–1474.
30. Wang W, Samat OA, Ge Y, Ma L, Tuheti A, Zou S, Abuduwaili J. Quantitative soil wind erosion potential mapping for Central Asia using the Google Earth Engine platform. *Remote Sens*. 2020;12(20):3430.
31. Cuevas-Agulló E, Barriopedro D, García RD, Alonso-Pérez S, González-Alemán JJ, Werner E, Suárez D, Bustos JJ, García-Castrillo G, García O, et al. Sharp increase in Saharan dust intrusions over the western Euro-Mediterranean in February–March 2020–2022 and associated atmospheric circulation. *Atmos Chem Phys*. 2024;24:4083–4104.
32. Tsunekawa A, Guo B, Liu B, Yamanaka N, Du S. *Restoration and development of the degraded Loess Plateau, China*. Berlin (Germany): Springer; 2014.
33. Wang B, Ding Q. Global monsoon: Dominant mode of annual variation in the tropics. *Dyn Atmos Oceans*. 2008;44(3-4):165–183.
34. Zhang N, Wang G. Detecting the causal interaction between Siberian high and winter surface air temperature over Northeast Asia. *Atmos Res*. 2020;245:Article 105066.
35. Ginoux P, Prospero JM, Gill TE, Hsu NC, Zhao M. Global-scale attribution of anthropogenic and natural dust sources and their emission rates based on MODIS Deep Blue aerosol products. *Rev Geophys*. 2012;50(3):Article RG3005.
36. Shao Y, Wyrwoll KH, Chappell A, Huang J, Lin Z, McTainsh GT, Mikami M, Tanaka TY, Wang X, Yoon S. Dust cycle: An emerging core in Earth system science. *Geomorphology*. 2013;139:189–197.
37. Webb NP, Pierre C. Quantifying anthropogenic dust emissions. *Nat Sustain*. 2018;1(2):466–473.
38. Cui L, Shen Z, Liu Y, Yu C, Lu Q, Zhang Z, Gao Y, Nie T. Identification of driving forces for windbreak and sand fixation services in semiarid and arid areas: A case of Inner Mongolia. *China Prog Phys Geogr*. 2023;47(1):32–49.
39. Hong C, Liu C, Zou X, Li H, Kai L, Liu B, Li J. Wind erosion rate for vegetated soil cover: A prediction model based on surface shear strength. *Catena*. 2020;187:Article 104398.
40. Yu W, Ma X, Wang Y, Yan W, Luo C, Han Y, Fan B. Simulating wind prevention and sand fixation service flow in arid inland river basins: Insights from the Tarim River basin. *China Sci Total Environ*. 2025;959:Article 178241.
41. Bergametti G, Rajot JL, Pierre C, Bouet C, Marticorena B. How long does precipitation inhibit wind erosion in the Sahel? *Geophys Res Lett*. 2016;43(12):6643–6649.
42. Zhou J, Liu Q, Liang L, Yan D, Yang Y, Wang X, Sun T, Li S, Gan L, Wu J. Water constraints enhanced by revegetation while alleviated by increased precipitation on China's water-dominated Loess Plateau. *J Hydrol*. 2024;636:Article 131202.
43. Zhao H, Zhang F, Yu Z, Li J. Spatiotemporal variation in soil degradation and economic damage caused by wind erosion in Northwest China. *J Environ Manag*. 2022;314:Article 115121.
44. You Y, Zhou N, Wang Y. Comparative study of desertification control policies and regulations in representative countries of the Belt and Road Initiative. *Glob Ecol Conserv*. 2021;21: Article e01577.
45. Zhu Y, Zheng Y, Zhao G, Zhu J, Zhao B, Sun Y, Gao J, Zhang Y. Evapotranspiration increase is more sensitive to vegetation greening than to vegetation type conversion in arid and semi-arid regions of China. *Glob Planet Change*. 2025;244:Article 104634.
46. Yu Y, Mao J, Wullschleger SD, Chen A, Shi X, Wang Y, Hoffman FM, Zhang Y, Pierce E. Machine learning-based observation-constrained projections reveal elevated global socio-economic risks from wildfire. *Nat Commun*. 2022;13(1):1250.
47. Ma D, Peng S, Lin Z. Towards a more comprehensive scenario analysis: Response of soil erosion to future land use and climate change in the Central Yunnan Urban Agglomeration, China. *J Environ Manage*. 2025;376:Article 124523.
48. Anderegg WRL, Trugman AT, Badgley G, Anderson CM, Bartuska A, Ciais P, Cullenward D, Field CB, Freeman J, Goetz SJ, et al. Climate-driven risks to the climate mitigation potential of forests. *Science*. 2020;368(6497):Article eaaz7005.

49. Yener İ. Development of high-resolution annual climate surfaces for Turkey using ANUSPLIN and comparison with other methods. *Atmósfera*. 2023;37:1–15.

50. Liu Q, Huang Z, Hu Z, Dong Q, Li S. Long-range transport and evolution of Saharan dust over East Asia from 2007 to 2020. *J Geophys Res Atmos*. 2022;127(18):e2022JD036974.

Ecosystem Health and Sustainability
A SCIENCE PARTNER JOURNAL

Spatiotemporal Dynamics and Cross-Regional Effects of Wind Erosion Prevention Services in Typical Arid–Semiarid Zone

Huilin Zhang, Zhitao Wu, Keming Ma, Hanxue Liang, Tianjie Lei, Ziqiang Du, and Xin Chen

Citation: Zhang H, Wu Z, Ma K, Liang H, Lei T, Du Z, Chen X. Spatiotemporal Dynamics and Cross-Regional Effects of Wind Erosion Prevention Services in Typical Arid–Semiarid Zone. *Ecosyst Health Sustain*. 2025;**11**:0449. DOI: 10.34133/ehs.0449

Wind erosion prevention service (WEPS) is critical for mitigating soil erosion and desertification in China's arid–semiarid zones. However, most existing studies have overlooked the spatial flow of WEPS, particularly the interannual variability and seasonal dynamics of sand transport pathways. This study focused on the loess hilly–gully region (LHGR), a climate-sensitive zone with intensified aeolian activity. We quantified the spatiotemporal dynamics of WEPS from 2000 to 2020 and simulated sand transport trajectories to assess cross-regional effects and socioeconomic dynamics. The results showed a marked increase in WEPS, indicating improved capacity of wind erosion prevention, with persistently high-value zones concentrated in northwestern arid regions such as the Mu Us Sandy Land. Wind trajectory identified 2,783 transport paths, dominated by spring winds (57.96%), which carried dust eastward toward densely populated areas and transboundary regions like Japan. Beneficiary areas exhibited a concentric spatial pattern, covering 599.96 × 104 km² (62.5% of China). The growing population, gross domestic product, and ecosystem service value highlighted its dual role in safeguarding human health and supporting sustainable development. Fraction vegetation coverage (FVC) emerged as the dominant factor for actual wind erosion by increasing surface roughness, with China's ecological restoration policies amplifying this function. Precipitation (PRE) predominantly regulated potential wind erosion, while synergistic interactions between FVC, PRE, and other drivers underscored the necessity for multi-factor governance. Our framework integrating physical flow and beneficiary mapping provides practical insights for optimizing payment for ecosystem service to enhance cross-regional ecological benefits.
Image

View the article online
https://spj.science.org/doi/10.34133/ehs.0449

Ecosystem Health and Sustainability (ISSN 2332-8878) is published by the American Association for the Advancement of Science. 1200 New York Avenue NW, Washington, DC 20005.